


Semiconductor-Quantum-Dot Modulator for Cryogenic Operation of Quantum Circuitry

M. R. Hogg^{1,*}, M.G. House^{1,2,†}, P. Pakkiam^{1,‡} and M.Y. Simmons^{1,2,§}

¹*Australian Research Council Centre of Excellence for Quantum Computation and Communication Technology, School of Physics, University of New South Wales, Sydney, New South Wales 2052, Australia*

²*Silicon Quantum Computing, Sydney, New South Wales 2052, Australia*

 (Received 15 February 2023; revised 6 July 2023; accepted 10 August 2023; published 27 September 2023)

Future large-scale quantum computing devices based on semiconductor spin qubits require multiplexed microwave control signals for manipulation and readout of the qubits. However, interfacing these control signals between room temperature and cryogenic temperatures where the qubits operate is a complex technical challenge. Here, we show a microwave modulator based on a nanoengineered semiconductor quantum dot that is designed to operate at millikelvin temperatures alongside the qubits. We operate the modulator as a mixer and a frequency multiplier over a bandwidth of up to 25 GHz. We estimate the power dissipation when driving quantum gates using frequency-up-converted signals under realistic experimental conditions to be 4 pW, highly compatible with the cooling powers available in current commercial dilution refrigerators. The device is fabricated in silicon using atomic precision lithography, providing a pathway toward combining qubits and classical control functionality on the same integrated chip.

DOI: [10.1103/PhysRevApplied.20.034066](https://doi.org/10.1103/PhysRevApplied.20.034066)

I. INTRODUCTION

Future large-scale solid-state quantum computing architectures will require high-bandwidth control and readout signals to perform computation and error correction [1–3]. Spin-qubit devices based on semiconductor quantum dots are a leading platform for quantum processing devices [4–7] and are typically operated at cryogenic temperatures. Currently, the signals required to control these qubits have most commonly been generated using room-temperature electronics. The electrical connections between room-temperature and cryogenic stages must, however, maintain signal integrity for high-carrier-frequency signals (up to tens of gigahertz) [8] without creating a heat load larger than the available cooling power. As computing devices scale to larger qubit numbers, more electrical connections are required, making interfacing room-temperature control signals with the cryogenic quantum processor an increasingly complex technical challenge [9].

An alternative strategy is to operate the qubit-control electronics at cryogenic temperatures directly [10,11],

thereby reducing the thermal gradient and the physical distance over which signals must travel. Significant progress has been made using classical cryo-CMOS devices for qubit control [12–14], motivating the search for novel signal generation and manipulation devices also operating at cryogenic temperatures. One intriguing prospect is to use quantum dot devices similar to those used to host the qubits. Here, dispersive-readout experiments on semiconductor quantum dots have demonstrated that the admittance behaves as a nonlinear capacitance [15,16]. Indeed, this nonlinear capacitance has recently been recognized as a useful novel circuit element, with a quantum dot based parametric amplifier being proposed [17] and later demonstrated experimentally [18]. The nonlinear capacitance of a quantum dot is analogous to the nonlinear inductance of Josephson junctions in superconducting circuits, which have been used to demonstrate quantum limited microwave amplifiers [19], switches [20], and circulators [21,22], as well as mixers and phase shifters [23]. Quantum dot based devices should thus be able to demonstrate similar functionality for semiconductor qubits, with the added advantage of resilience to the magnetic fields required for spin-qubit operation.

In this work, we consider a semiconductor quantum dot (tunnel coupled to a single lead) as an ultralow-dissipation wide-bandwidth nonlinear circuit element. We demonstrate operation of the quantum dot as a microwave mixer with an input bandwidth of over 25 GHz and as a frequency multiplier. Mixers form important building

*Present address: Department of Physics, The University of Basel, 4056 Basel, Switzerland.

†Present address: PsiQuantum Ltd., Palo Alto, California 94304, USA.

‡Present address: School of Mathematics and Physics, The University of Queensland, 4067 Brisbane, Australia.

§michelle.simmons@unsw.edu.au

blocks in microwave circuitry, as critical components in qubit-control electronics such as phase-sensitive detectors, vector signal generators, and amplifiers [24]. The low power dissipation (we estimate <4 pW) is fully compatible with millikelvin operation in a dilution refrigerator, where spin qubits have demonstrated the highest gate fidelities [25–27]. Previous experiments have investigated the use of metallic single-electron transistors (SETs) as microwave mixers [28–30]. In these experiments, the SETs have been operated in a multiterminal configuration that has modulated the resistance of the SET channel, hence dissipating power. In contrast, our quantum dot modulator is a reactive circuit element with power dissipation asymptotically approaching zero in the limit of high tunnel rates [31,32]. Reactive circuit elements (which do not have a resistive component to their impedance) are advantageous for millikelvin operation, as they do not dissipate power or introduce thermal noise. Our modulator is directly compatible with atom-scale spin-qubit fabrication technologies, providing a promising route to a hybrid quantum classical integrated circuit.

II. DEVICE DESIGN

We fabricate the device on a silicon substrate using a scanning tunneling microscope (STM) to perform atomic precision hydrogen-resist lithography [33,34]. Figure 1 shows an image of the device, in which the regions inside the white dotted lines have been selectively desorbed of hydrogen. The desorbed regions are then doped with phosphorus, giving rise to metallic conduction at millikelvin temperatures [35]. The device consists of a quantum dot (QD) tunnel coupled to a single reservoir lead (R) and capacitively coupled to a control gate (G). Atomic precision lithography allows nanoscale geometrical engineering, which we take advantage of by patterning a circular wraparound gate to maximize capacitive coupling with the quantum dot [36]. This geometry results in a gate lever arm (defined as $\alpha = C_i/C_\Sigma$, where C_i is the QD- G capacitance and C_Σ is the sum of all capacitances to QD) of $\alpha = 0.35$ (determined by measuring the Coulomb-peak width as a function of the temperature [15]). This value is the highest lever arm for a gate (excluding tunnel-coupled reservoirs) measured to date in STM-fabricated planar devices. Increasing α enhances the nonlinearity and increases modulator output amplitude. The fact that the phosphorus donors provide natural confining potentials for the electrons in the device means that additional confinement gates, which would complicate device operation and reduce the capacitive interaction between the gate G and QD [37], are not required. Based on the size of the QD (approximately 280 nm²), we estimate that 400–500 ³¹P donors will incorporate and electrical measurements show that the QD is large enough to be in the “metallic” dot regime (Appendix B). Based on COMSOL simulations, we

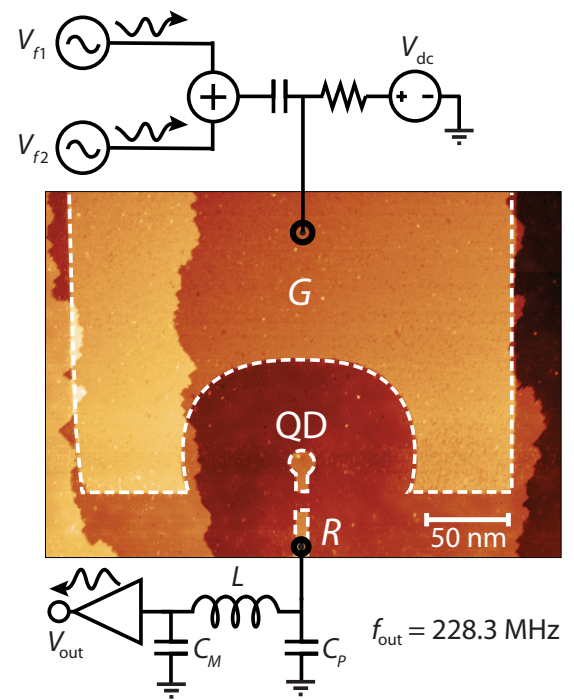


FIG. 1. An STM image of the quantum dot microwave modulator. The device consists of a quantum dot (QD) tunnel coupled to a single electron reservoir lead (R) and capacitively coupled to a circular gate (G) geometrically engineered to maximize the lever arm. The reservoir is coupled to a resonant impedance-matching circuit (L, C_P, C_M) that brings the high impedance of the device closer to 50Ω at 228.3 MHz. Bias tees on the reservoir and gate lines allow both dc and rf signals to be applied. Signals V_{f1} and V_{f2} can be applied to G individually (for frequency multiplication and dispersive measurements) or simultaneously (for mixing experiments).

expect the stray capacitance between G and R in our device to be approximately 13 aF.

As shown in Fig. 1, the reservoir lead is attached to a resonant LC circuit providing impedance matching between the device and the $50\text{-}\Omega$ coaxial cable routed to the measurement electronics. We apply one or more input signals of arbitrary frequency to the gate, while the output is always measured from the reservoir terminal at the resonant frequency f_{out} of the matching circuit. The output signals are amplified before acquisition on a spectrum analyzer.

III. THEORY OF OPERATION

We first introduce the theory required to understand the operation of the quantum dot as a mixer and frequency multiplier. Because of Coulomb blockade, the charge occupation of a quantum dot as a function of the gate voltage is a series of discrete steps with period E_c/α , where E_c is the charging energy [Fig. 2(a)]. Considering the region around one single charge-degeneracy point

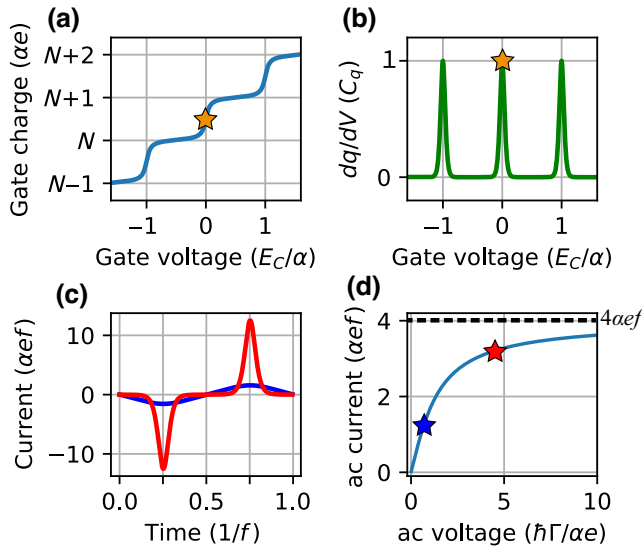


FIG. 2. Theory of quantum dot nonlinear admittance. (a) Average gate charge as a function of the gate voltage, showing discrete steps due to Coulomb blockade. (b) Differential capacitance of the quantum dot. When biased near a charge-degeneracy point (orange star), the device presents a nonlinear admittance and can be used as a mixer. (c) Average current over one ac voltage cycle for voltage amplitude $0.5V_0$ (blue line) and $4V_0$ (red line). (d) Absolute value of the ac current Fourier component at the driving frequency as a function of the drive amplitude. Saturation is observed at large drive amplitudes. Drive amplitudes for the red and blue curves in (c) are indicated by the corresponding colored stars.

(taken to be at $V_G = 0$ V), the average gate charge is given by

$$q(V_G) = \frac{\alpha e}{\pi} \arctan\left(\frac{V_G}{V_0}\right), \quad (1)$$

for the case of a lifetime-broadened charge transition ($\hbar\Gamma \gg k_B T$), where $V_0 = \hbar\Gamma/\alpha e$ is a characteristic voltage scale determining the half width at half maximum of a Coulomb peak (α is the lever arm of the gate, e is the electron charge, and Γ is the R to QD tunnel rate). The differential capacitance is given by

$$\frac{dq}{dV_G} = \frac{C_q}{1 + (V_G/V_0)^2}, \quad (2)$$

where $C_q = \alpha^2 e^2 / \pi \hbar \Gamma$ is the quantum capacitance [38, 39]. Equations (1) and (2) are plotted for multiple charge transitions in Figs. 2(a) and 2(b), respectively. In general, V_G has a dc bias component and an ac component, $V_G = V_{dc} + V_{ac} \cos(2\pi ft)$. When biased with a gate voltage V_{dc} near to a charge-degeneracy point [as shown by the orange stars in Figs. 2(a) and 2(b)], the device presents a nonlinear admittance and can be used as a mixer.

The current flowing in the device is the time derivative of the charge, $I = dq/dt$. At the charge-degeneracy point ($V_{dc} = 0$), a small sinusoidal voltage ($V_{ac} \ll V_0$) applied to the gate causes a sinusoidal current to flow, as shown by the blue curve in Fig. 2(c). In this regime, the admittance is $i\omega C_q$. For $V_{ac} \gtrsim V_0$ the admittance becomes nonlinear due to the discreteness of the quantum dot charging and the current no longer remains sinusoidal, shown by the red trace in Fig. 2(c). In this case, the current is concentrated around the times at which the charge-degeneracy point is crossed, giving rise to higher harmonics in the Fourier composition of the current. The device is thus acting as a frequency multiplier by generating new harmonics from a purely sinusoidal input voltage. We derive an expression for the Fourier component of the current at the drive frequency (Appendix C), given by

$$I_{ac}(f) = -4i\alpha ef \left(\frac{\sqrt{1 + (V_{ac}/V_0)^2} - 1}{V_{ac}/V_0} \right), \quad (3)$$

which saturates to a maximum amplitude of $|I_{ac}| = 4\alpha ef$, where f is the input frequency. Figure 2(d) plots this expression with the drive amplitudes from Fig. 2(c) indicated by red and blue stars. Intuitively, once an electron is being pumped on and off the quantum dot every ac cycle, the current component at the drive frequency cannot increase further (unless the input signal becomes larger than the charging energy of the QD, allowing multiple electrons to contribute; see Appendix F). This single-electron current generates the dispersive signal in a spin-qubit readout experiment; hence the saturation behavior determines the maximum achievable dispersive signal. We quantify this signal by estimating the maximum power that can result from the saturation value of I_{ac} , driven into an impedance matched to the dot impedance ($Z_{dot} = (i\omega C_q)^{-1}$), given by

$$P_{max} = \left| \frac{I_{ac}^2 Z_{dot}}{2} \right| = 4f \hbar \Gamma. \quad (4)$$

Equation (4) expresses the maximum possible dispersive signal generated by a single electron tunneling between a reservoir and a quantum dot, which follows directly from the saturation of I_{ac} . Note that while the lever arm α does not appear in this theoretical expression, in experiments, engineering a larger α increases C_q (for fixed Γ), thus reducing the device impedance and making impedance matching to 50Ω less technically challenging.

In the limit that $V_{ac} \gg V_0$ and $\Gamma \gg Nf$, we also derive an analytic expression for the current flowing at higher harmonics (Appendix C),

$$I_{ac}(Nf) = 4i\alpha ef (-1)^N \sin \left[N \arccos \left(\frac{V_{dc}}{V_{ac}} \right) \right], \quad (5)$$

for $|V_{dc}| < V_{ac}$, where N is the harmonic ($N = 1$ is the drive frequency). Note that for $V_{ac} \gg V_0$, the maximum current saturates to $4\alpha ef$ for all higher harmonics. This puts a theoretical upper limit on the output current of the frequency multiplier, which is important when considering potential applications such as frequency up-converting signals on chip to drive quantum gate operations via electron spin resonance (ESR) or electric dipole spin resonance (EDSR). Using these theoretical results, we can model our experimental results and predict the ultimate performance limits of our modulator under experimentally feasible conditions.

IV. RESULTS

Using the above understanding, we can calibrate our input and output signals *in situ* as voltage (V_{ac}) and current (I_{ac}) at the device. This allows us to abstract away details of the attenuations and gains in the experimental setup and focus purely on device-level inputs and outputs for direct comparison between theoretical and experimental results [15]. To do this, we measure the dispersive response sweeping V_{dc} over a single Coulomb peak as a function of the ac signal amplitude, applied to the gate at frequency f_{out} . Figure 3(a) shows the measured data (plotted as the signal amplitude above the background level, denoted by Δ in Fig. 3) for a range of input voltages V_{in} . Note that we use V_{in} to refer to the voltage output from the room-temperature signal generator and V_{ac} to refer to the voltage that reaches the device after cable losses and attenuation (all ac voltages are zero to peak).

Equation (5) with $N = 1$ describes the power broadening of the Coulomb peak. For each V_{in} value, we fit to an equation of the same form (given by $\Delta = \Delta_0 \sin[\arccos(V_{dc}/V_{ac})]$), with V_{ac} and Δ_0 as fitted parameters. Performing this fitting process yields -18 dB of attenuation between the signal generator and the device, similar to (within 1 dB) of the attenuation measured through the same cabling at room temperature. Figure 3(b) shows an example of this fit at the positions indicated by the white dashed horizontal line cuts in Fig. 3(a) at $V_{in} = 33$ mV and $V_{in} = 15$ mV. Both line cuts are in the saturation regime for I_{ac} (when $V_{ac} \gg V_0$), which explains why the larger drive amplitude does not result in a higher output signal (which would be expected for $V_{ac} < V_0$).

With V_{ac} calibrated, we use Eq. (3) to calibrate I_{ac} . Figure 3(c) shows a plot along $V_{dc} = 0$ V in Fig. 3(a), with a fit to an equation given by $\Delta = \Delta_{sat}(\sqrt{1 + (V_{ac}/V_0)^2} - 1)/(V_{ac}/V_0)$ (blue line), which has the same form as Eq. (3). Δ_{sat} and V_0 are fitted parameters, where Δ_{sat} is the measured output voltage in the saturation regime. The theoretical maximum current flowing is given by $|I_{sat}| = 4\alpha ef$, which for our experimental parameters is 51 pA. From the fit in Fig. 3(c), 51 pA of current at the device corresponds to $\Delta = 3.8$ mV measured at the spectrum

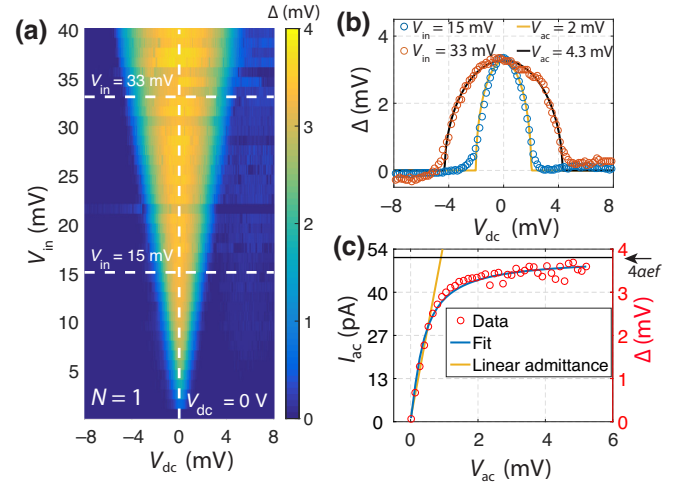


FIG. 3. Calibration of the device-level voltages and currents. (a) Measured dispersive signal sweeping V_{dc} over one Coulomb peak as a function of increasing drive amplitude V_{in} (here, $f_{in} = f_{out} = 228.3$ MHz). Δ is the measured signal level after performing a background subtraction. (b) Data (circles) and fits (solid lines) to Eq. (5) (with $N = 1$) for V_{in} values of 15 and 33 mV, indicated by horizontal dashed lines in (a). The fit gives corresponding values for V_{ac} shown in the legend. (c) Data (red circles) for $V_{dc} = 0$ V [vertical dashed line cut in (a)] expressed in terms of V_{ac} and I_{ac} (the current at the device). The blue line is a fit to Eq. (3), from which we calibrate the single-electron tunneling current (left-hand axis) and extract an estimate of the dot-to-reservoir tunnel coupling of $2\pi \times 25 \pm 5$ GHz. The black horizontal line shows the theoretical maximum current and the yellow linear admittance plot shows the expected response for a quantum capacitance of $\alpha^2 e^2 / \pi \hbar \Gamma$.

analyzer. Using this conversion, Fig. 3(c) plots the data with the left y -axis scale corresponding directly to current at the device. Using these calibrations, we can now express the rest of our experimental results directly in terms of device-level voltages and currents, I_{ac} and V_{ac} . From the fit in Fig. 3(c), we can also estimate the QD-to-R tunnel rate from the fitted parameter $V_0 (= \hbar\Gamma/\alpha e)$, which we find to be $\Gamma = 2\pi \times 25 \pm 5$ GHz. To demonstrate the relevance that our theory has to dispersive readout of spin qubits, we calculate the upper bound of the dispersive signal expected for our experimental parameters using Eq. (4). We find the maximum possible power derivable from the dispersive signal in this experiment to be $P_{max} = -108$ dBm. The noise floor in readout experiments is typically set by the noise temperature of the first-stage amplifier, for which current commercially available models is 4 K or less. Assuming a 4 K noise temperature, the maximum possible signal-to-noise ratio to detect the dispersive signal in our experiment is 27.6 dB at 500 kHz bandwidth (we choose 500 kHz as this is the theoretical bandwidth of the impedance-matching circuit, which transforms our device impedance perfectly to 50 Ω). This

detection sensitivity means that the integration time for a signal-to-noise ratio of 2 is 14 ns, comparable to the highest sensitivity charge detection demonstrated in semiconductor qubits [40]. Equation (4) states that the sensitivity can be increased with both higher tunnel coupling (Γ) and operating frequency (f).

Next, we demonstrate how we can operate the same device as a frequency multiplier by applying a single tone at a subharmonic of the impedance-matching circuit resonant frequency ($f_{\text{in}} = f_{\text{out}}/N$). The nonlinear admittance of the QD leads to harmonic generation. The impedance-matching circuit functions as a band-pass filter around f_{out} . Figure 4(a) shows experimental data for $N = 3$ as a function of V_{dc} (swept over a single Coulomb peak) and V_{ac} (swept from $V_{\text{ac}} < V_0$ to $V_{\text{ac}} > V_0$). At the values of V_{dc} for which an output is observed, the device is operating as a frequency tripler. Figure 4(b) is a theoretical plot of the expected output current, with the only input parameters being the experimentally measured tunnel rate, the lever arm, and an estimate of the temperature. The theory quantitatively reproduces the multilobed structure of the frequency-multiplier output observed in the experimental data. Figures 4(c) and 4(e) show data for $f_{\text{in}} = f_{\text{out}}/4$ and $f_{\text{in}} = f_{\text{out}}/5$, respectively [with corresponding theory plots in Figures 4(d) and 4(f)], with the device operating as a frequency quadrupler and quintupler. The QD-to-R tunnel rate puts a limit on the maximum frequency that can be generated by this multiplication process (which is $\Gamma = 2\pi \times 25 \pm 5$ GHz for this device). In future devices, tunnel rates of $2\pi \times 40\text{--}50$ GHz (in the range of ESR frequencies for ^{31}P at the approximately 1.5 T magnetic fields required for high-fidelity spin readout) should be possible by reducing the distance between R and QD.

As an example of the suitability of such a frequency multiplier to drive high-fidelity quantum gate operations, we use reported literature values for the voltage required to drive EDSR in a phosphorus-donor-based qubit system [41]. We find that Rabi oscillations at a frequency of 6 MHz (equivalently, a $\pi/2$ qubit rotation time of approximately 40 ns) should be possible for the conditions described in Ref. [41] (0.5-T magnetic field, 14-GHz qubit drive frequency) using the $N = 5$ output of a device engineered to have $\alpha = 0.7$ and $\Gamma = 2\pi \times 50$ GHz and being driven with a 20-mV signal at 2.8 GHz (for further details, see Appendix G). Using a simple rate-equation model [42], we estimate that under these conditions, approximately 4 pW of power would be dissipated due to nonadiabatic tunneling. A reasonable estimate for the resistance of the phosphorus-doped leads connecting to the quantum dot is 10 k Ω , meaning that a further 26 aW would be dissipated in the leads. In total, this is a small fraction of the cooling power available at the mixing chamber of a dilution refrigerator (units with 1 mW of cooling power at 100 mK are commercially available), indicating that scale-up prospects

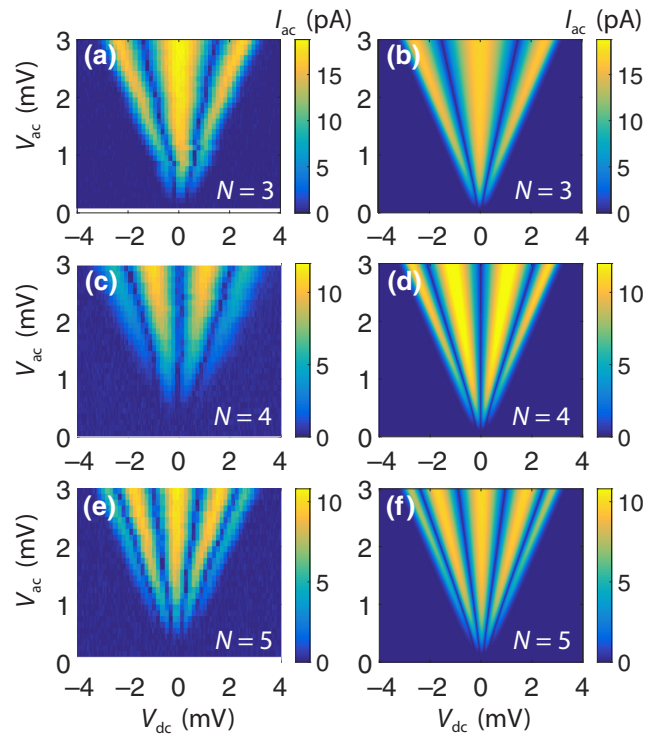


FIG. 4. Frequency multiplication by the quantum dot. With input frequency $f_{\text{in}} = f_{\text{out}}/N$, the measured output corresponds to the N th harmonic generated by the QD nonlinearity. Here, we show the measured data (left-hand column) and the theoretical prediction (right-hand column) for input signals of (a),(b) $N = 3$, (c),(d) $N = 4$, and (e),(f) $N = 5$.

for quantum dot frequency multipliers in terms of thermal budget are promising.

We now turn to operating the same device as a microwave mixer. Potential applications for spin qubits include developing millikelvin-operating quadrature demodulators (which are commonly used for qubit readout [16]), and to modulate spin-resonance signals for qubit control. In this experiment, we perform three-wave mixing by applying two signals to the gate (of amplitudes V_{f_1} and V_{f_2} at corresponding frequencies f_1 and f_2 in Fig. 1). The mixer generates output signals at the sum and difference frequencies ($f_1 - f_2$ and $f_1 + f_2$) as well as higher harmonics. In this instance, we measure the difference-frequency component by setting $f_1 - f_2 = f_{\text{out}}$. We keep $f_1 - f_2$ constant because of the impedance-matching circuit on R (Fig. 1); however, f_1 and f_2 can otherwise be varied arbitrarily [29].

Figure 5(a) presents data of the difference frequency output for $f_1 = 842.22$ MHz and $f_2 = 613.92$ MHz, measured as a function of the dc voltage (again over a single Coulomb peak) and amplitude V_{f_2} . V_{f_1} serves as the local oscillator (LO) for the mixer and is fixed at 3.5 mV in Fig. 5(a). Figure 5(b) demonstrates the effect of the dc bias voltage on the mixer output. Choosing a bias voltage

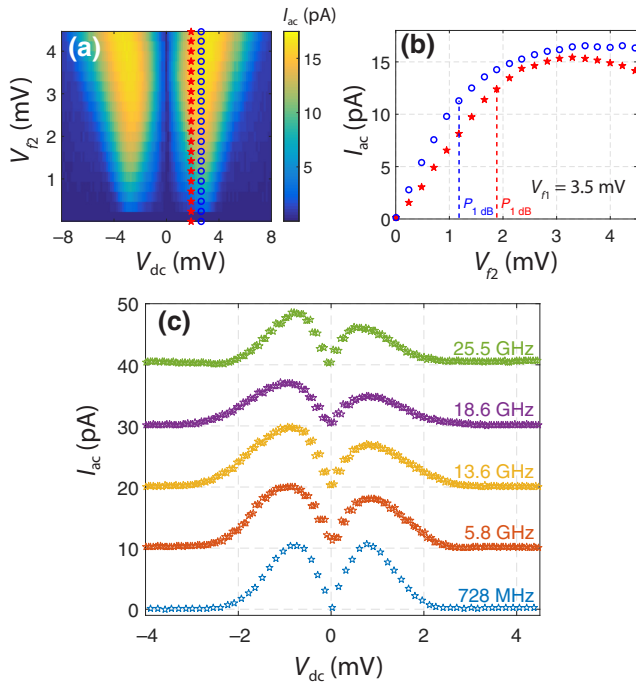


FIG. 5. Input power and frequency dependence of the quantum dot mixer output. (a) The current measured at the difference frequency $f_1 - f_2$ for $f_1 = 842.22$ MHz and $f_2 = 613.92$ MHz as a function of V_{dc} and V_{f_2} . V_{f_1} is fixed at 3.5 mV and functions as the local oscillator for the mixer. Mixing output is observed when the dc bias is set to the side of the Coulomb peak, as here the nonlinear admittance permits three-wave mixing. The blue circles and red stars indicate two different dc bias points that change the mixer output characteristics, as shown in (b). (b) The dependence of the mixer output on the dc operating point. Choosing $V_{dc} = V_{LO}$ maximizes mixer output (blue circles), however choosing a value of $V_{dc} < V_{LO}$ increases the input range over which the output is linear. $P_{1\text{ dB}}$ indicates the input amplitude for which the output deviates from linearity by 1 dB (the 1 dB compression point) for the corresponding data. (c) The output of the mixer measured up to gigahertz frequencies. We measure the mixer output for input frequencies of $f_c = 728$ MHz and 5.8, 13.6, 18.6, and 25.5 GHz, where f_c is the center input frequency. Output is still clearly observed at the difference frequency for $f_c = 25.5$ GHz. The data at $f_c = 728$ MHz matches the frequency condition for the data in (a) and (b). The traces are offset by 10 pA for clarity.

V_{dc} equal to the LO voltage maximizes the mixer output amplitude (blue circles); however, setting $V_{dc} < V_{LO}$ maximizes the range of input amplitudes for which the mixer output is linear (red stars). Depending on the application, different dc bias conditions might be utilized. The precise values chosen for f_1 and f_2 in this experiment are representative, with similar results being shown over a wide range of frequencies.

To demonstrate the achievable bandwidth of the mixer, we increase both f_1 and f_2 to gigahertz frequencies (still maintaining $f_1 - f_2 = f_{out}$). Figure 5(c) shows the mixing

output at f_{out} taken while sweeping V_{dc} over one Coulomb peak for input signals with varying center frequency $f_c = 728$ MHz and 5.8, 13.6, 18.6, and 25.5 GHz, where $f_c = (f_1 + f_2)/2$. In these measurements, $V_{f_1} = V_{f_2} \sim 2$ mV. The dataset at 728 MHz is at the same frequency as the data in Fig. 5(a). The asymmetry of the mixer output over a Coulomb peak at the highest frequencies is reproduced in our numerical model by assuming asymmetric tunnel in and out rates, the effect of which is more pronounced as f_c becomes comparable to the lower tunnel rate (Appendix E).

We observe down-converted output from the mixer up to input frequencies of 25.5 GHz, promising for future on-chip modulation applications that will require modulating signals in the megahertz-to-gigahertz range for qubit readout and tens of gigahertz for quantum gates. The fact that STM-fabricated gates can respond to applied frequencies of approximately 25 GHz is also promising for future fault-tolerant designs using this technology, which require precisely timed pulses synchronized across parallel gates [1]. Previous experiments have demonstrated STM-fabricated gates operating up to 13 GHz [43]—our results significantly extend this; however, further work is required to precisely measure the propagation characteristics of two-dimensional (2D) phosphorus-doped leads deep into gigahertz frequencies. Our numerical simulations show that signal output from the mixer is no longer possible if the *output* frequency (i.e., $f_1 - f_2$ or $f_1 + f_2$ if generating the sum frequency) approaches the tunnel rate (the input frequencies can actually exceed it; see Appendix E). The tunnel rate thus sets the ultimate limit on mixer bandwidth, implying that sum-or-difference-frequency output should be possible up to approximately 25 GHz in the present device. For further STM-fabricated devices, this frequency limit can be increased by moving the QD and R closer together, thereby increasing the tunnel rate. A tunnel rate of 50 GHz would mean modulation of quantum gate drive signals (typically 30–40 GHz for single ^{31}P donors in silicon [44]) should be achievable.

V. CONCLUSIONS

Using atomic precision hydrogen-resist lithography, we have fabricated a quantum dot microwave modulator with a geometry engineered at the nanoscale to maximize gate lever arm. In contrast to previous STM-fabricated devices [45–47], this device is intended to advance classical control and readout at millikelvin temperature rather than host qubits. We have demonstrated that the admittance of the tunnel-coupled quantum dot is nonlinear and we have used this nonlinear admittance as a resource to operate the device both as a frequency multiplier and a microwave mixer. We have shown that the mixer can generate output over a wide input frequency range up to approximately 25 GHz, limited in this device by the QD-to-R tunnel

rate. Based on a theoretical analysis, we predict that when operated as a frequency multiplier, the device could also generate output up to approximately 25 GHz, again limited by the tunnel rate. We have demonstrated how the theory used to describe the nonlinear nature of the quantum dot admittance is relevant to dispersive readout of spin qubits, as it reveals the fundamental limit on the achievable amount of signal. We have found that it should be possible to detect dispersive signals with a signal-to-noise ratio of 2 for an integration time of 14 ns using an ideal impedance-matching circuit, similar to the highest-sensitivity charge detection reported to date in semiconductor qubits. We have also calculated the power dissipated by the device and estimated that under realistic operating conditions for driving quantum gate operations in a phosphorus-donor qubit system, the device would dissipate approximately 4 pW of power. We note that although this number for power dissipation is a theoretical estimate, we have not observed any heating of the cryostat for experimental configurations expected to dissipate $\gg 4$ pW of power based on the same theory.

Our device is thus a low-dissipation reactive circuit element, fully compatible with millikelvin temperatures and readily integrable with fabrication techniques for semiconductor spin-based quantum computing devices. We note that although our present experimental setup is not equipped with a magnet, the magnitude of the quantum capacitance in a similar quantum dot–reservoir coupled system has been shown to be independent of the magnetic field [48], meaning that our device operation should be compatible with the fields typically required for spin-qubit operation. We also note that the mixer device that we demonstrate here could, in principle, be implemented with any quantum dot technology. STM lithography has some significant advantages that make scaling a large-scale modulator chip more geometrically tractable (specifically, a lower gate density and a smaller device footprint); however, in particular, nanowire devices with wraparound gates have demonstrated gate lever arms $\alpha > 0.9$, which would be beneficial for modulator performance [32]. Tunable tunnel barriers in gate-defined quantum dots would also allow adjustment of the modulator operation bandwidth, which is difficult for STM devices in which tunnel barriers are fixed at the time of fabrication. In the future, quantum dot based circuit elements such as mixers and parametric amplifiers could be integrated on the same chip as the qubits, to form a hybrid quantum classical integrated circuit.

ACKNOWLEDGMENTS

This research was conducted via the Australian Research Council Centre of Excellence for Quantum Computation and Communication Technology (Project No. CE170100012) and Silicon Quantum Computing Pty Ltd.

M.Y.S. acknowledges an Australian Research Council Laureate Fellowship. The device was fabricated in part at the NSW node of the Australian National Fabrication Facility (ANFF).

M.G.H. conceived the idea for the experiment. M.R.H. designed and fabricated the device. M.R.H. performed the measurements with assistance from M.G.H. M.R.H. and M.G.H. analyzed the data, with input from P.P. M.G.H. and P.P. developed the theory. M.R.H., M.G.H., and M.Y.S. wrote the manuscript, with input from P.P. M.G.H. and M.Y.S. supervised the project. M.Y.S. is a director of the company Silicon Quantum Computing Pty Ltd, and M.G.H. is the owner of a patent (WIPO Patent No. WO2018148784) describing a quantum dot based parametric amplifier that is related to the present work. All other authors declare no competing financial interests.

Note added.—We recently became aware of related work demonstrating frequency multiplication using a quantum dot [49].

APPENDIX A: DEVICE DETAILS AND MEASUREMENT SETUP

The device is fabricated using atomic precision lithography in an ultrahigh-vacuum (UHV) environment, then encapsulated with 50 nm of epitaxially grown silicon. After encapsulation, the device is removed from UHV and electrical connection is made to the phosphorus layer using aluminum ohmic contacts. Figure 1 shows a schematic of the key components of our measurement setup; here, we provide further details of the device and measurement setup. Figure 6 shows the full experimental configuration, including the details of all electrical components. The device is glued and bonded to a custom-designed printed circuit board (PCB) using a low-loss Rogers RO4003 laminate dielectric. The resonant impedance-matching circuit is formed by a surface-mount inductor ($L = 1200$ nH) together with the parasitic capacitance to ground ($C_p = 0.4$ pF), giving a resonance frequency of 228.3 MHz. A parallel capacitor ($C_M = 39$ pF) is added to complete a π -matching filter. With the device bonded, the resonator has a quality factor of $Q \sim 120$ when cooled to cryogenic temperatures. The dc voltages to the device terminals are supplied via bias-tee circuits that are external to the main-device PCB. For the gate voltage, a Pasternack PE1621 bias tee (located at room temperature outside the cryostat) is used to combine dc and rf voltages (up to 40 GHz) to the gate. For the reservoir voltage, a hand-soldered RC bias tee ($R = 10$ k Ω , $C = 220$ pF, target cutoff frequency of approximately 70 kHz), located inside the cryostat on an additional PCB, is used to combine dc and rf voltages to the gate. The transmission pathway between the aluminum ohmic contacts and the device bond pads is designed to form a coplanar waveguide impedance matched to 50 Ω for high-frequency signal transmission. The signal tracks on

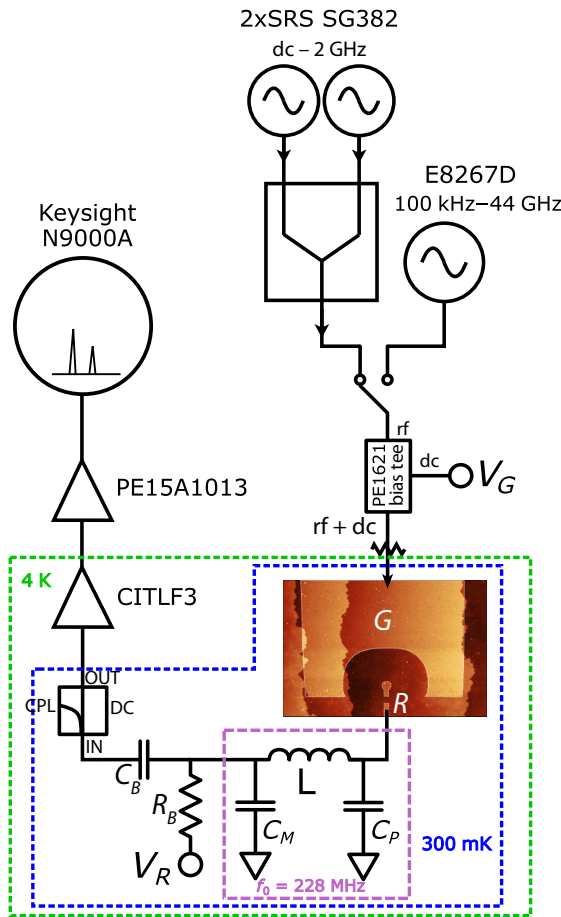


FIG. 6. The full measurement configuration. The ac signals are supplied to the device gate (G) using either SRS SG382 signal generators (for frequencies < 2 GHz) or a Keysight E8267D vector signal generator (for frequencies > 2 GHz). The dc signals are supplied to the gate via a Pasternack PE1621 bias tee. The resonant impedance-matching circuit is formed by an inductor ($L = 1200$ nH) and the parasitic capacitance of the circuit ($C_P \sim 0.4$ pF), together with an additional capacitor ($C_M = 39$ pF) to form a π -matching circuit. A bias tee is also connected to the reservoir lead (R) to allow dc voltages to be applied and ac voltages to be transmitted ($C_B = 220$ pF, $R_B = 10$ k Ω , cut-off frequency of approximately 70 kHz). The signal from the reservoir side is amplified at 4 K and room temperature, before being acquired on a spectrum analyzer (Keysight N9000A). A directional coupler (DC) provides the option of performing reflectometry measurements.

the PCB are also designed to be 50- Ω impedance matched. The device PCB is enclosed within a custom-designed copper box and cooled down to approximately 300 mK in a sorption-pumped ^3He refrigerator. The refrigerator cannot maintain base temperature continuously and in our experiments has an average “hold time” of approximately 4 h, followed by a recondensing cycle of approximately 40 min to return to base temperature.

APPENDIX B: QUANTUM DOT CHARGING ENERGY AND LEVER ARMS

Figure 7(a) shows a 2D map acquired in reflectometry, sweeping the gate voltage versus the reservoir voltage. Regular Coulomb peaks are observed when the Fermi energy of the reservoir is aligned with an available charge state on the QD, a charge-degeneracy point. The black dashed line in Fig. 7(a) has a slope of exactly one, which matches almost exactly the slope of the charge-degeneracy lines. The slope of the charge-degeneracy lines is related to the lever arms of the gate and reservoir terminals acting on the QD. The lever arm of lead i is defined by $\alpha_i = C_i/C_\Sigma$, where $C_\Sigma = \sum_i C_i$ is the total sum capacitance. The slope of the charge-degeneracy line is given by

$$\frac{\Delta V_R}{\Delta V_G} = \frac{\alpha_G}{1 - \alpha_R}, \quad (\text{B1})$$

where α_G is the gate lever arm and α_R is the reservoir lever arm. The fact that the slope of the charge-degeneracy line is equal to one in our experiment means that $\alpha_G + \alpha_R = 1$, from which it follows directly that $C_G + C_R = C_\Sigma$, i.e., that the only two contributions to the QD total capacitance are from the gate and reservoir terminals.

Figure 7(b) shows a line cut through multiple Coulomb peaks [with 0.076 V applied to the reservoir terminal in Fig. 7(a)]. The spacing between Coulomb peaks (i.e., the addition voltage E_c/α_G) is extremely regular, with a spacing of 16.7 ± 0.4 mV. The fact that our addition voltage is very consistent over multiple Coulomb peaks demonstrates that our QD is large enough to be in the “metallic” dot regime.

APPENDIX C: DERIVATION OF ANALYTIC EXPRESSIONS USED IN THE MAIN TEXT

In the main text, we have introduced Eq. (3) to describe the Fourier component of the current at the drive frequency when the quantum dot is driven by a sinusoidal voltage and Eq. (5) which describes the power broadening of a Coulomb peak. Here, we provide brief derivations for both of these analytic expressions.

To derive Eq. (5), we use a simple model that is valid in the limit of large driving amplitude ($V_{ac} \gg V_0$). In this regime, the ac voltages applied are much greater than the line width of the charge transition and the charge-voltage relation of the circuit near one charge transition (taken to be at $V_{dc} = 0$) is approximately a Heaviside step function,

$$q(V) = \alpha e \Theta(V). \quad (\text{C1})$$

We further assume that the tunnel rate Γ is much faster than the driving frequency f ($\Gamma \gg f$), such that an electron charge responds instantaneously to a change in voltage. In this regime, when the gate is driven by voltage $V_G(t) =$

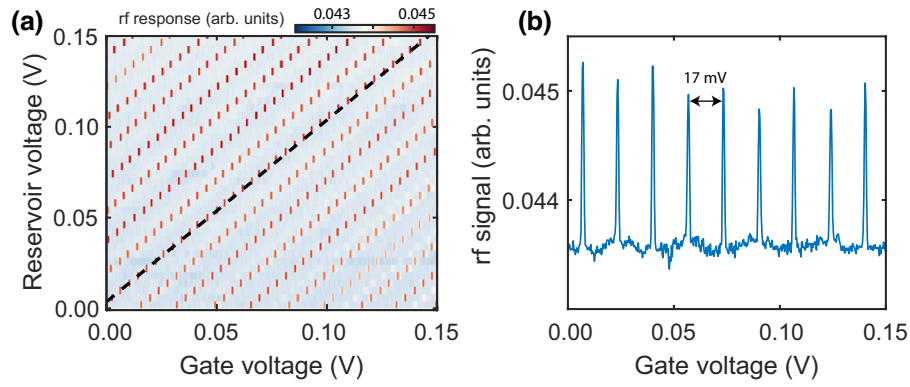


FIG. 7. The quantum dot Coulomb peaks. (a) A gate versus reservoir voltage scan, showing regular Coulomb peaks at QD charge-degeneracy positions. The dashed black line has a slope of exactly one (closely matching the QD transition line slope), showing that the only relevant capacitive couplings to the QD are from gate and reservoir terminals. (b) A line cut at $V_R = 0.076$ V. Over a 150-mV range, the QD addition voltage is highly regular, indicating that the QD is in the metallic regime.

$V_{dc} + V_{ac} \cos(2\pi ft)$ the resulting current is a series of delta functions,

$$I(t) = \frac{d}{dt} q[V_G(t)] = \alpha e \left\{ \delta \left[t - \frac{1}{2\pi f} \arccos \left(\frac{-V_{dc}}{V_{ac}} \right) \right] - \delta \left[t - \frac{1}{f} + \frac{1}{2\pi f} \arccos \left(\frac{-V_{dc}}{V_{ac}} \right) \right] \right\}, \quad (C2)$$

for $|V_{ac}| < |V_{dc}|$. The Fourier amplitude of the current at the N th harmonic frequency is

$$\begin{aligned} I(nf) &= 2if \int_0^{f^{-1}} \sin(2\pi nft) I(t) dt \\ &= 4i\alpha e f (-1)^n \sin \left[n \arccos \left(\frac{V_{dc}}{V_{ac}} \right) \right] \\ &= 4i\alpha e f (-1)^n \sqrt{1 - \left(\frac{V_{dc}}{V_{ac}} \right)^2} U_{n-1} \left(\frac{V_{dc}}{V_{ac}} \right), \quad (C3) \end{aligned}$$

where $U_{n-1}(x)$ is the Chebyshev polynomial of the second kind. The first few harmonics are

$$\begin{aligned} I(f) &= -4i\alpha e f \sqrt{1 - \left(\frac{V_{dc}}{V_{ac}} \right)^2}, \\ I(2f) &= 4i\alpha e f \sqrt{1 - \left(\frac{V_{dc}}{V_{ac}} \right)^2} \left[2 \left(\frac{V_{dc}}{V_{ac}} \right) \right], \\ I(3f) &= -4i\alpha e f \sqrt{1 - \left(\frac{V_{dc}}{V_{ac}} \right)^2} \left[4 \left(\frac{V_{dc}}{V_{ac}} \right)^2 - 1 \right], \\ I(4f) &= 4i\alpha e f \sqrt{1 - \left(\frac{V_{dc}}{V_{ac}} \right)^2} \left[8 \left(\frac{V_{dc}}{V_{ac}} \right)^3 - 4 \left(\frac{V_{dc}}{V_{ac}} \right) \right]. \quad (C4) \end{aligned}$$

The absolute values of these expressions are plotted in Fig. 8, for comparison with the experimental data in Fig. 3. The model reproduces the multinodal structure of the harmonic responses, with the model accurately reproducing the experimental data in the limit of large $|V_{ac}|$. At smaller voltages, the step-function approximation breaks down and the currents measured are smaller than predicted by this model. However, fitting the expression for the first harmonic in Eq. (C4) to the data is an accurate way to calibrate V_{ac} as a function of V_{in} , as described in the main text.

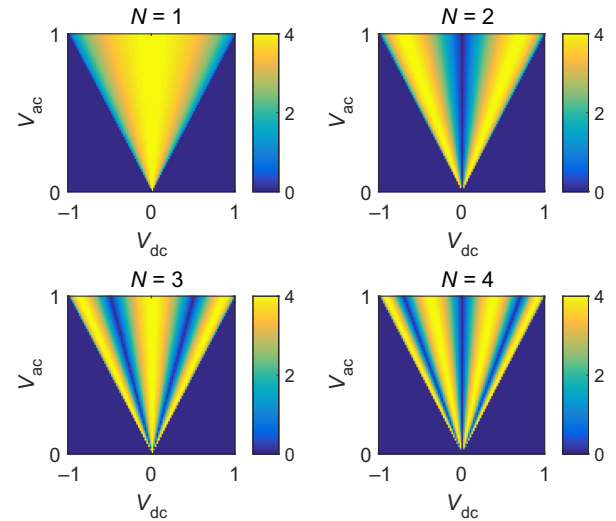


FIG. 8. The harmonic responses of the quantum dot frequency multiplier predicted by step-function approximation. The absolute values of the Fourier components of the current at $N = 1, 2, 3, 4$ harmonics [calculated from Eq. (C3)] are plotted as a function of a dc offset voltage from a charge degeneracy V_{dc} and ac voltage V_{ac} . The voltage units are arbitrary. The current amplitude is expressed in units of $\alpha e f$.

To derive Eq. (3), we start from the charge-voltage relation for a lifetime-broadened charge transition [Eq. (1)],

$$q(V_G) = \frac{\alpha e}{\pi} \arctan\left(\frac{V_G}{V_0}\right), \quad (\text{C5})$$

where V_0 is a characteristic voltage scale defined in the main text. Assuming $V_{dc} = 0$, we then have $V_G = V_{ac} \cos(\omega t)$. We substitute this into Eq. (C5) and taken the Fourier integral over a single period, which results in an analytic expression:

$$q(\omega) = \frac{\omega}{\pi} \int_0^{2\pi/\omega} q(t) \cos(\omega t) dt \quad (\text{C6})$$

$$= \frac{2\alpha e}{\pi} \left(\frac{-1 + \sqrt{1 + (V_{ac}/V_0)^2}}{V_{ac}/V_0} \right). \quad (\text{C7})$$

The current is given by the time derivative of the charge (i.e., $I(\omega) = -i\omega q(\omega)$),

$$I(\omega) = -4i\alpha e f \left(\frac{\sqrt{1 + (V_{ac}/V_0)^2} - 1}{V_{ac}/V_0} \right), \quad (\text{C8})$$

which is Eq. (3). With V_{ac} calibrated using the first harmonic of Eq. (C4), fitting this expression to the experimental data along a line cut at $V_{dc} = 0$ is an accurate way of calibrating I_{ac} , as outlined in the main text.

APPENDIX D: NUMERICAL MODELING OF MIXER OUTPUT

When operating the device as a mixer by applying two signals of noncommensurate frequencies f_1, f_2 to give a

time-varying voltage

$$V_G(t) = V_{dc} + V_1 \cos(2\pi f_1 t) + V_2 \cos(2\pi f_2 t), \quad (\text{D1})$$

it is more difficult to derive an analytic formula for the mixer output current, so we calculate it numerically. In this appendix, we show that our numerical modeling of the mixer is consistent with the experimental data. We show the result of such a calculation in Fig. 9. As there is no absolute voltage scale in this model, we can summarize the voltage dependence of the mixing output in terms of ratios of the voltages. In Fig. 9(a), we show a calculation of the output current at frequency $f_{out} = f_2 - f_1$ as a function of dc offset V_{dc}/V_2 and ac amplitude V_1/V_2 . Here, we choose $f_2 = 3.6891f_{out}$ and $f_1 = 2.6891f_{out}$ to match the frequency relationships of Fig. 5(a). The result shown here compares well with the experimentally measured results in Fig. 5(a). In Fig. 9(b), we show the same information replotted as a function of the two input amplitudes V_1 and V_2 relative to a fixed V_{dc} . The maximum mixing output is for voltages $V_1 = V_2 \approx V_{dc}$.

The mixer can perform up-conversion mixing (where the output is then at $f_{out} = f_1 + f_2$) as well as the down-conversion mixing discussed in the main text. From the numerical calculations, we also observe that the current at frequency $f_{out} = f_2 \pm f_1$ is proportional to f_{out} but otherwise independent of the input frequencies f_1 and f_2 . To illustrate this, we plot in Fig. 9(c) the current at f_{out} for $V_{dc} = V_1 = V_2$ as a function of $f_c = (f_2 + f_1)/2$ for down-conversion mixing [the orange curve in Fig. 9(c)] and $f_d = (f_2 - f_1)/2$ for up-conversion mixing [the blue curve in Fig. 9(c)]. The center frequency f_c for down-conversion mixing is the same as that defined in the main text and we define f_d for up-conversion mixing as a parameter that can be varied while f_{out} is kept fixed. The result shows that independent of the input frequencies and whether the desired output is up-conversion or down-conversion, the output amplitude is

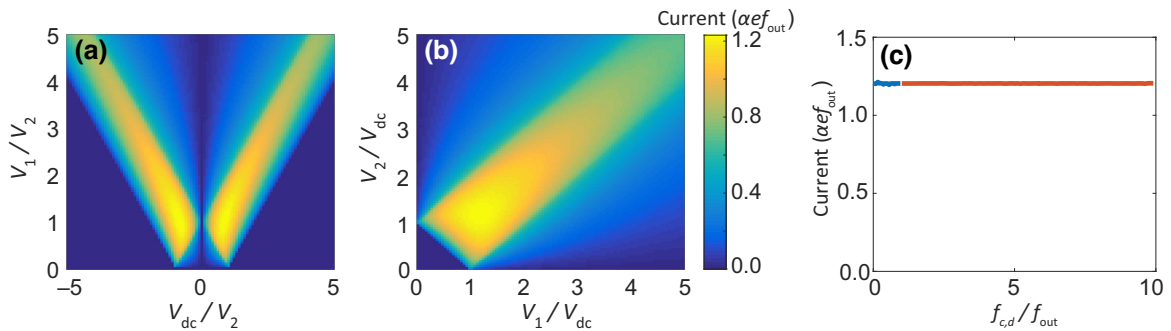


FIG. 9. Numerical modeling of the mixer output. (a) The dependence of the mixing output current at frequency $f_{out} = f_2 - f_1$ on the dc offset V_{dc} and ac amplitude V_1 for a fixed V_2 . This corresponds to Fig. 5(a). (b) The same as in (a) but plotted as a function of V_1, V_2 relative to a fixed V_{dc} . The maximum output occurs when $V_1 = V_2$. (c) The frequency dependence of the mixing output as a function of $f_c = (f_2 + f_1)/2$ for down-conversion mixing for fixed f_{out} (orange curve) and $f_d = (f_2 - f_1)/2$ for up-conversion mixing (blue curve). We observe that the mixing output amplitude is independent of the input frequencies chosen provided that their sum or difference is equal to f_{out} .

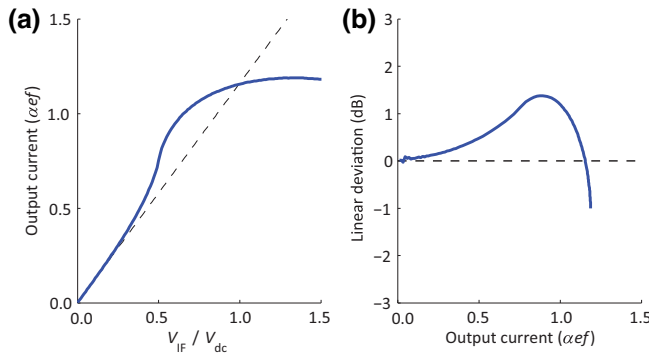


FIG. 10. Linearity of the mixer output current with respect to the IF signal amplitude. (a) The calculated output current at frequency $f_{\text{IF}} = f_{\text{IF}} + f_{\text{LO}}$ as a function of the “intermediate-frequency” amplitude V_{IF} when applying a dc bias V_{dc} and fixed local oscillator tone of amplitude V_{LO} at frequency f_{LO} . The dashed line indicates a perfectly linear response for comparison. (b) The calculated up-conversion output, expressed in dB units relative to a perfectly linear response. The response is linear to within about 1 dB, up to the saturation of the output at about $1.2\alpha e f_{\text{IF}}$.

the same, approximately $1.2\alpha e f_{\text{out}}$. This is also consistent with experimental observations.

One figure of merit for the up-conversion and down-conversion mixing processes is the linearity of the modulated output with respect to one input signal. For example, given an input signal $V_{\text{IF}}(t)$ (which is to be up-converted to frequency $f_{\text{IF}} = f_{\text{IF}} + f_{\text{LO}}$ using a fixed dc bias point V_{dc} , local oscillator of frequency f_{LO} and amplitude V_{LO}), over what input range is the output linear. Using the model described above, we find the conversion process to have the largest range of linearity when $V_{\text{LO}} > V_{\text{dc}}$ [as shown in the experimental data in Fig. 5(b)]. This is illustrated

in Fig. 10(a), which shows the converted output signal as a function of a smaller intermediate-frequency signal V_{IF} for $V_{\text{LO}} = 1.5V_{\text{dc}}$, the same data as a vertical cut through Fig. 9(b) at $V_1/V_{\text{dc}} = 1.5$. The deviation of the output from its initial linear trend is expressed in units of dB in Fig. 10(b). We see that up to the saturation of the output (approximately $1.2\alpha e f_{\text{IF}}$) it remains linear to within about 1.5 dB.

APPENDIX E: FINITE-TUNNEL-RATE EFFECTS: DISSIPATION, MIXER BANDWIDTH, AND BIAS ASYMMETRY

The theory in Appendixes A–D assumes that the electron tunnels instantaneously in response to the changing gate voltage or, equivalently, that the electron tunnel rate is much greater than the operating frequencies of the mixer. We can relax this assumption to understand the effect of finite tunnel rates, dissipation, and the bandwidth limitations of the mixer. Now assume that an electron tunnels stochastically with a fixed average rate $\Gamma_{\text{in}}/2\pi$ to tunnel into the dot and $\Gamma_{\text{out}}/2\pi$ to tunnel out. Then, the time-averaged charge on the gate obeys the rate equation

$$\frac{d}{dt} \langle q \rangle = \begin{cases} \frac{\Gamma_{\text{in}}}{2\pi} (\langle q \rangle - \alpha e), & \text{for } V_G(t) > 0, \\ -\frac{\Gamma_{\text{out}}}{2\pi} \langle q \rangle, & \text{for } V_G(t) < 0. \end{cases} \quad (\text{E1})$$

For a steady-state single-tone input signal $V(t) = V_{\text{dc}} + V_{\text{ac}} \cos(\omega t)$, this equation has an analytic solution, which we do not reproduce here in full because of its complexity, but in the simple case $V_{\text{dc}} \rightarrow 0$, $\Gamma_{\text{in}} = \Gamma_{\text{out}} \rightarrow \Gamma$, the solution is

$$\langle q \rangle (t) = \begin{cases} \alpha e \frac{1}{1 + \exp(-\frac{\Gamma}{2\omega})} \exp(-\frac{\Gamma}{2\pi} t + \frac{\pi}{2\omega}), & \text{for } \frac{\pi}{2} \leq t < \frac{3\pi}{2}, \\ \alpha e \left[1 - \frac{1}{1 + \exp(\frac{\Gamma}{2\omega})} \exp(-\frac{\Gamma}{2\pi} t + \frac{5\pi}{2\omega}) \right], & \text{for } 0 \leq t < \frac{\pi}{2}, \frac{3\pi}{2} \leq t < 2\pi. \end{cases} \quad (\text{E2})$$

The average power dissipated is

$$\begin{aligned} \langle P \rangle &= \frac{2\pi}{\omega} \int_0^{\frac{2\pi}{\omega}} V_{\text{ac}} \cos(\omega t') \frac{d\langle q \rangle}{dt'} dt' \\ &= V_{\text{ac}} \frac{\alpha e \omega}{\pi} \frac{2\pi \omega \Gamma}{\Gamma^2 + (2\pi \omega)^2}. \end{aligned} \quad (\text{E3})$$

The analytic expression for the power dissipation with nonzero dc bias is very complicated but it has the approximate dependence $\langle P \rangle \propto \sqrt{1 - (V_{\text{dc}}/V_{\text{ac}})^2}$, the same bias

dependence as the current [Eq. (C4)]. We use the expression given in Eq. (E3) to calculate the power dissipated during a frequency-multiplier application in the main text, putting in the numbers $\omega = 2\pi \times 2.8$ GHz, $\alpha = 0.7$, $V_{\text{ac}} = 20$ mV, which results in $\langle P \rangle = 4$ pW.

In the main text, we state that the ultimate bandwidth limit of the mixer is determined by the QD to R tunnel rate Γ . We state that output is no longer observed when the output frequency approaches Γ and that the input frequencies f_1 and f_2 can actually exceed Γ . In this appendix, we provide evidence for this statement using a

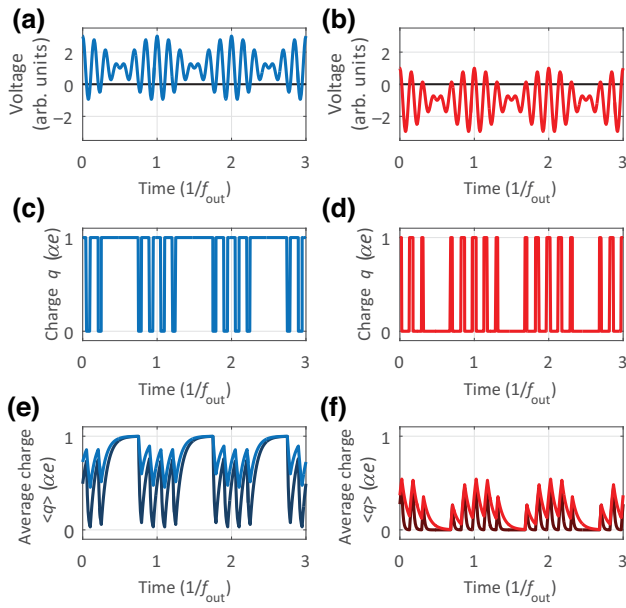


FIG. 11. The mixer response in the time domain with finite-tunnel-rate effects. (a) An example of a down-conversion mixer input voltage in arbitrary units, $V(t) = 1 + \cos(2\pi \times 6t) + \cos(2\pi \times 7t)$. The output frequency is assumed to be $f_{\text{out}} = 1$. (b) The same plot as (a) but for a negative dc bias voltage. (c) The charge response of the quantum dot to the input voltage shown in (a), assuming tunnel rates much faster than the input frequencies. (d) A plot similar to (c) for the negative dc bias wave form shown in (b). (e) The charge response of the quantum dot with the effects of finite tunnel rates included. The light-blue curve shows the average charge response assuming equal tunnel on and off rates, $\Gamma_{\text{in}} = \Gamma_{\text{out}} = 2\pi \times 2f_{\text{out}}$. The dark-blue curve shows that when the tunnel-out rate is increased to $\Gamma_{\text{out}} = 2\pi \times 10f_{\text{out}}$, the charge oscillations (and therefore the mixer output) are enhanced. (f) The same simulation as in (e) but assuming negative dc bias. The red curve assumes equal tunnel on and off rates. The brown curve is for asymmetric tunnel rates, which leads to a suppression of the charge oscillations.

numerical model describing the time dynamics of electron tunneling when an input of two signals is applied, $V_G(t) = V_{\text{dc}} + V_1 \cos(2\pi f_1 t) + V_2 \cos(2\pi f_2 t)$. Figure 11(a) shows a few cycles of $V_G(t)$ for $V_{\text{dc}} = V_1 = V_2 = 1$ and $f_1 = 6$, $f_2 = 7$. We consider a down-conversion mixing process at frequency $f_{\text{out}} = f_2 - f_1 = 1$ and we see the beating pattern, which has slow frequency f_{out} . During part of the beat period, the combined ac voltages are too small to reach the charge transition at $V = 0$ and the charge remains localized on the quantum dot, near times $t \approx 0.5, 1.5, 2.5, \dots$. In the other part of the beat period, the electron is pumped back and forth rapidly, as shown in Fig. 11(b) near times $t \approx 1, 2, 3, \dots$. The Fourier component of the charge oscillations at frequency f_{out} is insensitive to these fast oscillations, at approximately $f_1 + f_2$, which is why the total mixer output current is proportional to the output frequency f_{out} but nearly independent of the input frequencies f_1, f_2 .

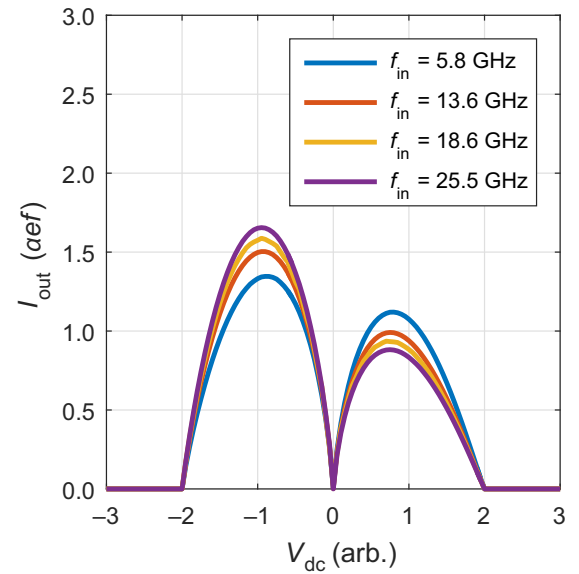


FIG. 12. The numerical modeling of the asymmetric mixer output current due to finite-tunnel-rate effects. The simulated mixer output as a function of the dc bias, for direct comparison with Fig. 5(c), assuming asymmetric tunnel rates $\Gamma_{\text{in}} = 2\pi \times 25 \text{ GHz}$ and $\Gamma_{\text{out}} = \Gamma_{\text{in}}/2$.

The light-blue trace in Fig. 11(e) shows the average steady-state charge response of the quantum dot in response to the applied voltage of Fig. 11(a), averaged over many oscillation periods, given tunnel rates $\Gamma_{\text{in}} = \Gamma_{\text{out}} = 2\pi \times 2f_{\text{out}}$. The finite tunnel rate has the effect of applying a low-pass filter, which averages over the fast oscillations but has little effect on the Fourier component at frequency f_{out} , even when the input frequencies are faster than the tunnel rate. We note that in the case when f_1, f_2 are larger than the tunnel rate, although the average charge response is the same, the electron charge does not necessarily follow the voltage adiabatically and there could be dissipation and noise added to the mixing output.

We also suggest a possible explanation of the asymmetry of mixer output with respect to V_{dc} over a Coulomb peak that we observe in the experiment [seen in Fig. 5(c)]. We can reproduce this effect in our numerical model by assuming two distinct tunnel rates for an electron to tunnel on and off the quantum dot, $\Gamma_{\text{in}} \neq \Gamma_{\text{out}}$. We illustrate this with the dark-blue trace in Fig. 11(e), which is the same as the light-blue trace except we assume a faster tunnel-out rate, $\Gamma_{\text{out}} = 2\pi \times 10f_{\text{out}}$, but the same tunnel-in rate $\Gamma_{\text{in}} = 2\pi \times 2f_{\text{out}}$. Here, we see enhancement in the average charge oscillation because with this dc bias, the electron spends most its time on the quantum dot, so a faster tunnel-out rate leads to more “off” time, on average. By comparison, when the opposite dc bias is applied, $V_{\text{dc}} = -1$, as shown in Fig. 11(f), the average oscillation is reduced compared to the equal-tunnel-rate case.

To determine the impact a tunnel-rate asymmetry would have on our mixer device, we repeat the above simulation using the same input and output frequencies as in the experiment, assuming tunnel rates of $\Gamma_{\text{in}} = 2\pi \times 25$ GHz and $\Gamma_{\text{out}} = \Gamma_{\text{in}}/2$. The results, shown in Fig. 12, are roughly consistent with the experiment [Fig. 5(c)]. We speculate that a factor-of-2 difference in the tunnel-in compared to the tunnel-out rate could be due to the dot ground state having a spin degeneracy of 2 but it could also be due to nonuniform density of states in the reservoir or the quantum dot itself. The tunnel rates may also not be independent of the gate voltage as we have assumed.

APPENDIX F: MULTIELECTRON DRIVING AT LARGE ac VOLTAGES

In the main text, we have worked in a regime where only a single electron is contributing to the tunneling process and our theoretical analysis assumes this to be the case. However in our device, we have also observed multielectron tunneling when operating the device as a frequency multiplier, by applying a large enough ac voltage amplitude to exceed the charging voltage of our quantum dot. In this case, the ac voltage spans more than one Coulomb peak and multiple electrons can contribute to the output current. Figure 13 shows experimental data obtained using $N = 12$ over a range of V_{ac} values large enough to drive multiple electrons. An interference pattern is observed, with constructive addition to the current at some combinations of V_{dc} and V_{ac} and destructive at others. In the future, it may be possible to take advantage of constructive-interference effects to increase the maximum possible output current; however, we have not carefully studied this effect in this work. It is worth noting that the drive amplitude of 20 mV calculated for using the frequency multiplier to drive qubit gate operations (Appendix G) actually exceeds the charging voltage in the device studied here; however, in future devices, the charging voltage could be increased by reducing the size of the quantum dot.

APPENDIX G: CALCULATION OF ELECTRICALLY DRIVEN QUANTUM GATE OPERATION TIME

Here, we describe the method used to calculate the input voltage required to drive Rabi oscillations at a frequency of 6 MHz in an electrically driven donor qubit system, the results of which are described in the main text. EDSR is popular in semiconductor spin-based quantum computing devices [50,51] due to the ease of applying electric fields localized at the nanoscale compared to the magnetic fields used for magnetically driven spin resonance. We use the parameters of Ref. [41], as this provides a comprehensive study of EDSR in a donor-based system.

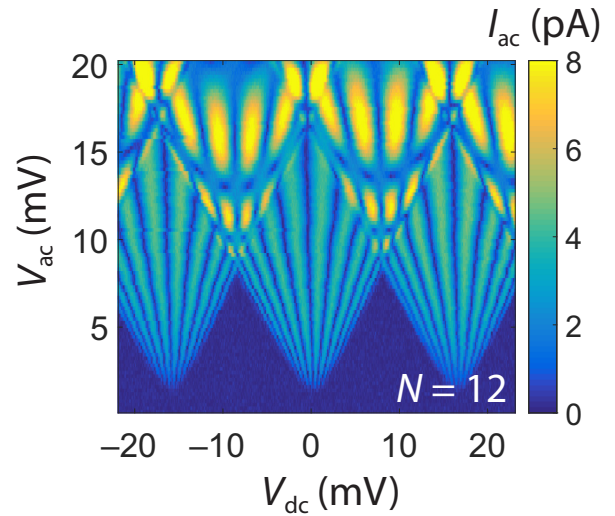


FIG. 13. Frequency multiplication with $N = 12$ and strong ac driving. When V_{ac} exceeds the charging voltage of the quantum dot (given by E_c/α), multiple electrons can contribute to the output current, leading to the interference effects observed here.

Specifically, Ref. [41] considers two tunnel-coupled donor quantum dots separated by 11.4 nm. The application of a magnetic field of 0.5 T causes Zeeman splitting of the energy levels of an electron bound to one of the donors. If an alternating electric field is applied to the system, the electron is shuttled backward and forward between the two donor quantum dots, experiencing an effective alternating magnetic field due to the difference in hyperfine interactions strengths between the two quantum dots. If the frequency of the applied electric field matches the Zeeman energy, the electron spin undergoes Rabi oscillations. In Ref. [41], an electric field of 15 kV/m is shown to drive Rabi oscillations at approximately 6 MHz frequency for a Zeeman splitting of 14 GHz. A device similar to the frequency multiplier described in the main text could be used to up-convert an input signal at a lower frequency to a frequency matching the spin-resonance condition. The output of the frequency multiplier would then be transmitted to a gate, which would electrically drive the qubit system. An electric field of 15 kV/m corresponds to a voltage of $450 \mu\text{V}$ applied to a gate located 30 nm from the donor-based qubit system, which is straightforward to fabricate using atomic precision lithography. For an input to the frequency multiplier at 2.8 GHz, we use a numerical solver to estimate that an input signal amplitude of 20 mV would be required to generate an output voltage of $450 \mu\text{V}$ at 14 GHz. This is the value quoted in the main text.

It should also be noted that in the main text it is stated that magnetic fields of 1.5 T are required for single-spin qubits (meaning approximately 40-GHz qubit drive frequencies); however, this is assuming that qubit readout is performed by spin-selective tunneling to an electron

reservoir [52]. In Ref. [41], spin-selective tunneling to an ancillary quantum dot is instead used for qubit readout, which relaxes the requirement that the Zeeman splitting be greater than thermal broadening in the reservoir. Lower magnetic fields (and hence lower qubit drive frequencies) can be used in this case.

APPENDIX H: ALTERNATIVE CHARGE-TRANSITION LINE SHAPES

In the device used in our measurements, the Coulomb peaks are lifetime broadened, so that the line shape (average charge occupancy of the quantum dot as a function of gate voltage) is determined by the tunnel coupling to a Fermi sea of electrons with uniform density of states, which leads to a Lorentzian shape (we see evidence of asymmetry in the tunnel-in and tunnel-out rates, so the Lorentzian line shape may be an oversimplification; however, the exact line shape does not change the performance of the mixer qualitatively, particularly for large input amplitudes).

Another possible line shape in devices with smaller tunnel couplings or operating at higher temperatures is primarily determined by thermal broadening, when $k_B T \gg \hbar\Gamma$. In this case, the charge-voltage relationship is

$$q(V) = \frac{\alpha e}{2} \left[1 + \tanh\left(\frac{\alpha e}{2k_B T} V\right) \right]. \quad (\text{H1})$$

The same analysis as in the main text applies, with the parameter replacements

$$C_q = \frac{\alpha^2 e^2}{4k_B T}, \quad V_0 = \frac{2k_B T}{\alpha e}. \quad (\text{H2})$$

The admittance of the quantum dot, its nonlinear behavior, and the performance of the mixer are all qualitatively the same in this regime.

Another case we can consider is that the gate addresses a charge transition between two quantum dots. Modeling these as a two-level quantum system with tunnel coupling between the dots t_c and Hamiltonian $\hat{H} = -\alpha e V / 2\hat{\sigma}_z + t_c \hat{\sigma}_x$, and assuming the electron always remains in the ground state of the system, the gate-reservoir charge-voltage relation is

$$q(V) = \frac{\alpha e}{2} \left[1 + \frac{\frac{\alpha e}{2t_c} V}{\sqrt{1 + \left(\frac{\alpha e}{2t_c}\right)^2 V^2}} \right]. \quad (\text{H3})$$

Here, the capacitance and voltage scales are

$$C_q = \frac{\alpha^2 e^2}{2t_c}, \quad V_0 = \frac{2t_c}{\alpha e}. \quad (\text{H4})$$

Again there is no significant qualitative difference between this case and the one discussed in the main text. The

response will be different if the charge state behaves nonadiabatically under the influence of the driving voltage, which will happen when the drive frequency is comparable to the tunnel coupling.

-
- [1] C. D. Hill, E. Peretz, S. J. Hile, M. G. House, M. Fuechsle, S. Rogge, M. Y. Simmons, and L. C. L. Hollenberg, A surface code quantum computer in silicon, *Sci. Adv.* **1**, e1500707 (2015).
 - [2] M. H. Devoret and R. J. Schoelkopf, Superconducting circuits for quantum information: An outlook, *Science* **339**, 1169 (2013).
 - [3] J. M. Taylor, H. A. Engel, W. Dür, A. Yacoby, C. M. Marcus, P. Zoller, and M. D. Lukin, Fault-tolerant architecture for quantum computation using electrically controlled semiconductor spins, *Nat. Phys.* **1**, 177 (2005).
 - [4] N. W. Hendrickx, W. I. L. Lawrie, M. Russ, F. van Riggelen, S. L. de Snoo, R. N. Schouten, A. Sammak, G. Scappucci, and M. Veldhorst, A four-qubit germanium quantum processor, *Nature* **591**, 580 (2021).
 - [5] S. G. J. Philips, M. T. Madzik, S. V. Amitonov, S. L. de Snoo, M. Russ, N. Kalhor, C. Volk, W. I. L. Lawrie, D. Brousse, L. Tryputen, B. P. Wuetz, A. Sammak, M. Veldhorst, G. Scappucci, and L. M. K. Vandersypen, Universal control of a six-qubit quantum processor in silicon, *Nature* **609**, 919 (2022).
 - [6] K. Takeda, A. Noiri, T. Nakajima, J. Yoneda, T. Kobayashi, and S. Tarucha, Quantum tomography of an entangled three-qubit state in silicon, *Nat. Nanotechnol.* **16**, 965 (2021).
 - [7] K. Takeda, A. Noiri, T. Nakajima, T. Kobayashi, and S. Tarucha, Quantum error correction with silicon spin qubits, *Nature* **608**, 682 (2022).
 - [8] S. Gustavsson, O. Zwiernik, J. Bylander, F. Yan, F. Yoshihara, Y. Nakamura, T. P. Orlando, and W. D. Oliver, Improving Quantum Gate Fidelities by Using a Qubit to Measure Microwave Pulse Distortions, *Phys. Rev. Lett.* **110**, 040502 (2013).
 - [9] L. M. K. Vandersypen, H. Bluhm, J. S. Clarke, A. S. Dzurak, R. Ishihara, A. Morello, D. J. Reilly, L. R. Schreiber, and M. Veldhorst, Interfacing spin qubits in quantum dots and donors—hot, dense, and coherent, *npj Quantum Inf.* **3**, 34 (2017).
 - [10] J. M. Hornibrook, J. I. Colless, I. D. Conway Lamb, S. J. Pauka, H. Lu, A. C. Gossard, J. D. Watson, G. C. Gardner, S. Fallahi, M. J. Manfra, and D. J. Reilly, Cryogenic Control Architecture for Large-Scale Quantum Computing, *Phys. Rev. Appl.* **3**, 024010 (2015).
 - [11] D. Rotta, F. Sebastiano, E. Charbon, and E. Prati, Quantum information density scaling and qubit operation time constraints of CMOS silicon-based quantum computer architectures, *npj Quantum Inf.* **3**, 26 (2017).
 - [12] E. Charbon, F. Sebastiano, A. Vladimirescu, H. Homulle, S. Visser, L. Song, and R. M. Incandela, in *2016 IEEE International Electron Devices Meeting (IEDM) (San Francisco, CA, USA, 2016)*, p. 13.5.1.
 - [13] X. Xue, *et al.*, CMOS-based cryogenic control of silicon quantum circuits, *Nature* **593**, 205 (2021).

- [14] A. Ruffino, T.-Y. Yang, J. Michniewicz, Y. Peng, E. Charbon, and M. F. Gonzalez-Zalba, A cryo-CMOS chip that integrates silicon quantum dots and multiplexed dispersive readout electronics, *Nat. Electron.* **5**, 53 (2022).
- [15] M. G. House, I. Bartlett, P. Pakkiam, M. Koch, E. Peretz, J. van der Heijden, T. Kobayashi, S. Rogge, and M. Y. Simmons, High-Sensitivity Charge Detection with a Single-Lead Quantum Dot for Scalable Quantum Computation, *Phys. Rev. Appl.* **6**, 044016 (2016).
- [16] P. Pakkiam, A. V. Timofeev, M. G. House, M. R. Hogg, T. Kobayashi, M. Koch, S. Rogge, and M. Y. Simmons, Single-Shot Single-Gate rf Spin Readout in Silicon, *Phys. Rev. X* **8**, 041032 (2018).
- [17] M. G. House, A parametric amplifier (WIPO Patent No. WO2018148784, August 2018). https://patentscope.wipo.int/search/en/detail.jsf?docId=WO2018148784&_cid=P20-LM6HIA-22517-1.
- [18] L. Cochrane, T. Lundberg, D. J. Ibberson, L. A. Ibberson, L. Hutin, B. Bertrand, N. Stelmashenko, J. W. A. Robinson, M. Vinet, A. A. Seshia, and M. F. Gonzalez-Zalba, Parametric Amplifiers Based on Quantum Dots, *Phys. Rev. Lett.* **128**, 197701 (2022).
- [19] C. Macklin, K. O'Brien, D. Hover, M. E. Schwartz, V. Bolkhovskiy, X. Zhang, W. D. Oliver, and I. Siddiqi, A near-quantum-limited Josephson traveling-wave parametric amplifier, *Science* **350**, 307 (2015).
- [20] B. J. Chapman, B. A. Moores, E. I. Rosenthal, J. Kerckhoff, and K. W. Lehnert, General purpose multiplexing device for cryogenic microwave systems, *Appl. Phys. Lett.* **108**, 222602 (2016).
- [21] K. M. Sliwa, M. Hatridge, A. Narla, S. Shankar, L. Frunzio, R. J. Schoelkopf, and M. H. Devoret, Reconfigurable Josephson Circulator/Directional Amplifier, *Phys. Rev. X* **5**, 041020 (2015).
- [22] J. Kerckhoff, K. Lalumière, B. J. Chapman, A. Blais, and K. W. Lehnert, On-Chip Superconducting Microwave Circulator from Synthetic Rotation, *Phys. Rev. Appl.* **4**, 034002 (2015).
- [23] O. Naaman, J. A. Strong, D. G. Ferguson, J. Egan, N. Bailey, and R. T. Hinkey, Josephson junction microwave modulators for qubit control, *J. Appl. Phys.* **121**, 073904 (2017).
- [24] D. M. Pozar, *Microwave Engineering* (Wiley, New York, 2005), 3rd ed.
- [25] X. Xue, M. Russ, N. Samkharadze, B. Undseth, A. Sammak, G. Scappucci, and L. M. K. Vandersypen, Quantum logic with spin qubits crossing the surface code threshold, *Nature* **601**, 343 (2022).
- [26] A. Noiri, K. Takeda, T. Nakajima, T. Kobayashi, A. Sammak, G. Scappucci, and S. Tarucha, Fast universal quantum gate above the fault-tolerance threshold in silicon, *Nature* **601**, 338 (2022).
- [27] M. T. Madzik, *et al.*, Precision tomography of a three-qubit donor quantum processor in silicon, *Nature* **601**, 348 (2022).
- [28] R. Knobel, C. S. Yung, and A. N. Cleland, Single-electron transistor as a radio-frequency mixer, *Appl. Phys. Lett.* **81**, 532 (2002).
- [29] D. J. Reilly and T. M. Buehler, Direct measurement of the intrinsic RC roll-off in a radio frequency single electron transistor operated as a microwave mixer, *Appl. Phys. Lett.* **87**, 163122 (2005).
- [30] L. J. Swenson, D. R. Schmidt, J. S. Aldridge, D. K. Wood, and A. N. Cleland, Mixing with the radio frequency single-electron transistor, *Appl. Phys. Lett.* **86**, 173112 (2005).
- [31] M. G. House, T. Kobayashi, B. Weber, S. J. Hile, T. F. Watson, J. van der Heijden, S. Rogge, and M. Y. Simmons, Radio frequency measurements of tunnel couplings and singlet-triplet spin states in Si:P quantum dots, *Nat. Commun.* **6**, 8848 (2015).
- [32] M. F. Gonzalez-Zalba, S. Barraud, A. J. Ferguson, and A. C. Betz, Probing the limits of gate-based charge sensing, *Nat. Commun.* **6**, 6084 (2015).
- [33] M. Simmons, F. Ruess, K. Goh, T. Hallam, S. Schofield, L. Oberbeck, N. Curson, A. Hamilton, M. Butcher, R. Clark, and T. Reusch, Scanning probe microscopy for silicon device fabrication, *Mol. Simul.* **31**, 505 (2005).
- [34] M. Fuechsle, J. A. Miwa, S. Mahapatra, H. Ryu, S. Lee, O. Warschkow, L. C. L. Hollenberg, G. Klimeck, and M. Y. Simmons, A single-atom transistor, *Nat. Nanotechnol.* **7**, 242 (2012).
- [35] K. E. J. Goh, L. Oberbeck, M. Y. Simmons, A. R. Hamilton, and M. J. Butcher, Influence of doping density on electronic transport in degenerate Si:P δ -doped layers, *Phys. Rev. B* **73**, 035401 (2006).
- [36] W. C. T. Lee, G. Scappucci, D. L. Thompson, and M. Y. Simmons, Development of a tunable donor quantum dot in silicon, *Appl. Phys. Lett.* **96**, 043116 (2010).
- [37] M.R. Hogg, P. Pakkiam, S.K. Gorman, A.V. Timofeev, Y. Chung, G.K. Gulati, M.G. House, and M.Y. Simmons, Single-Shot Readout of Multiple Donor Electron Spins with a Gate-Based Sensor, *PRX Quantum* **4**, 010319 (2023).
- [38] A. Prêtre, H. Thomas, and M. Büttiker, Dynamic admittance of mesoscopic conductors: Discrete-potential model, *Phys. Rev. B* **54**, 8130 (1996).
- [39] A. Cottet, C. Mora, and T. Kontos, Mesoscopic admittance of a double quantum dot, *Phys. Rev. B* **83**, 121311 (2011).
- [40] J. Stehlik, Y.-Y. Liu, C. M. Quintana, C. Eichler, T. R. Hartke, and J. R. Petta, Fast Charge Sensing of a Cavity-Coupled Double Quantum Dot Using a Josephson Parametric Amplifier, *Phys. Rev. Appl.* **4**, 014018 (2015).
- [41] Y. Wang, C.-Y. Chen, G. Klimeck, M. Y. Simmons, and R. Rahman, All-electrical control of donor-bound electron spin qubits in silicon, [arXiv:1703.05370](https://arxiv.org/abs/1703.05370) (2017).
- [42] F. Persson, C. M. Wilson, M. Sandberg, G. Johansson, and P. Delsing, Excess Dissipation in a Single-Electron Box: The Sisyphus Resistance, *Nano Lett.* **10**, 953 (2010).
- [43] G. C. Tettamanzi, S. J. Hile, M. G. House, M. Fuechsle, S. Rogge, and M. Y. Simmons, Probing the Quantum States of a Single Atom Transistor at Microwave Frequencies, *ACS Nano* **11**, 2444 (2017).
- [44] J. J. Pla, K. Y. Tan, J. P. Dehollain, W. H. Lim, J. J. L. Morton, D. N. Jamieson, A. S. Dzurak, and A. Morello, A single-atom electron spin qubit in silicon, *Nature* **489**, 541 (2012).
- [45] T. F. Watson, B. Weber, Y.-L. Hsueh, L. C. L. Hollenberg, R. Rahman, and M. Y. Simmons, Atomically engineered electron spin lifetimes of 30 s in silicon, *Sci. Adv.* **3**, e1602811 (2017).

- [46] S. J. Hile, L. Fricke, M. G. House, E. Peretz, C. Y. Chen, Y. Wang, M. Broome, S. K. Gorman, J. G. Keizer, R. Rahman, and M. Y. Simmons, Addressable electron spin resonance using donors and donor molecules in silicon, *Sci. Adv.* **4**, eaaq1459 (2018).
- [47] Y. He, S. K. Gorman, D. Keith, L. Kranz, J. G. Keizer, and M. Y. Simmons, A two-qubit gate between phosphorus donor electrons in silicon, *Nature* **571**, 371 (2019).
- [48] I. Ahmed, A. Chatterjee, S. Barraud, J. J. L. Morton, J. A. Haigh, and M. F. Gonzalez-Zalba, Primary thermometry of a single reservoir using cyclic electron tunneling to a quantum dot, *Commun. Phys.* **1**, 66 (2018).
- [49] G. A. Oakes, L. Peri, L. Cochrane, F. Martins, L. Hutin, B. Bertrand, M. Vinet, A. G. Saiz, C. J. B. Ford, C. G. Smith, and M. F. Gonzalez-Zalba, A quantum dot-based frequency multiplier, [arXiv:2211.14127](https://arxiv.org/abs/2211.14127) (2022).
- [50] T. F. Watson, S. G. Philips, E. Kawakami, D. R. Ward, P. Scarlino, M. Veldhorst, D. E. Savage, M. G. Lagally, M. Friesen, S. N. Coppersmith, M. A. Eriksson, and L. M. Vandersypen, A programmable two-qubit quantum processor in silicon, *Nature* **555**, 633 (2018).
- [51] D. M. Zajac, A. J. Sigillito, M. Russ, F. Borjans, J. M. Taylor, G. Burkard, and J. R. Petta, Resonantly driven CNOT gate for electron spins, *Science* **359**, 439 (2018).
- [52] A. Morello, J. J. Pla, F. a. Zwanenburg, K. W. Chan, K. Y. Tan, H. Huebl, M. Möttönen, C. D. Nugroho, C. Yang, J. a. van Donkelaar, A. D. C. Alves, D. N. Jamieson, C. C. Escott, L. C. L. Hollenberg, R. G. Clark, and A. S. Dzurak, Single-shot readout of an electron spin in silicon, *Nature* **467**, 687 (2010).